Supporting Information

Baish et al. 10.1073/pnas.1018154108

SI Discussion

1 Analytical Model of Diffusion. Here we seek approximate, analytical relationships for transient diffusion in the extravascular space surrounding the blood vessels. This is a particular case of diffusive transport through a homogeneous solid near an irregular boundary. The surface irregularities of interest here are sufficiently large that diffusion may be regarded as a macroscopic process. Our immediate interest is diffusion into blood vessels from the extravascular space, but the resulting approximation works well on a wide variety of geometries and may have other physical applications. Our present approach differs from that in the literature used to address problems of steady-state diffusion near an irregular surface (1) and also from situations in which anomalous diffusion may arise. Here we have diffusion through a compact, homogeneous substrate that has an irregular boundary, whereas anomalous diffusion results from heterogeneity in the underlying substrate (2).

We aim to approximate the full 3D problem with a 1D form of the transient diffusion equation that accounts for variation in the number of voxels $n(\delta)$ at a given distance δ from the vascular surface. This is a generalized formulation that reduces to the well-known forms appropriate for planar, cylindrical or spherical coordinates in special cases, but can also accommodate other forms of $n(\delta)$. We focus in particular on the power-law form $n(\delta) = n_1(\delta/l)^\lambda$ where l is the width of a voxel that can be fit, at least locally, to the actual variation obtained from images or various artificial geometries. Ultimately, we obtain a similarity solution for the rate of mass diffusion from the extravascular space into the blood vessels that can be used to evaluate several parameters of pharmacokinetic significance. Numerical simulations of various 2D and 3D geometries in *Numerical Solutions for Specific Geometries* demonstrate the validity of the analytical results that follow.

We begin by considering the general case of 3D transient diffusion in an extravascular space of arbitrary shape governed by

$$D_m \nabla^2 C(\vec{r},t) - R(\vec{r},t) = \frac{\partial C(\vec{r},t)}{\partial t}, \qquad \textbf{[S1]}$$

where $C(\vec{r},t)$ is the concentration as a function of position and time and $R(\vec{r},t)$ is the rate of elimination by metabolism or binding. Here we will consider only nonreactive tracers ($R(\vec{r},t) = 0$). Points on the blood vessel walls $\vec{r}_v$ form the boundary of the extravascular space. We assume that the concentration throughout the blood vessels is established on a shorter time scale than that pertaining to the diffusion process so that the concentration on the vessel walls may vary with time as $C_v(t)$ but is uniform with respect to position, that is $C(\vec{r}_v,t) = C_v(t)$. Whereas this assumption will not be strictly valid for highly diffusive molecules that may exhibit some flow-limited behavior, it is useful as a tool for examining the diffusive behavior of drugs or other tracers that take longer to diffuse from the vessels. We also recognize that the vessel wall might have a finite permeability, but our numerical simulations showed that the scaling behavior we report here differs only modestly from that obtained by using a uniform, effective diffusivity throughout the extravascular tissue. We further assume that the concentration is initially uniform throughout the extravacular tissue at $C(\vec{r},0) = C_i$.

Solutions for the preceding problem can be constructed from solutions of the following auxiliary problem

$$D_m \nabla^2 \Phi(\vec{r},t) = \frac{\partial \Phi(\vec{r},t)}{\partial t}, \qquad \textbf{[S2]}$$

subject to the boundary condition $\Phi(\vec{r}_v,t) = 1$ and the initial condition $\Phi(\vec{r},0) = 0$ using Duhamel's theorem as follows (3)

$$C(\vec{r},t) = C_i + \int_{\tau=0}^{t} C_v(t) \frac{\partial \Phi(\vec{r},t-\tau)}{\partial t} d\tau. \qquad \textbf{[S3]}$$

Because solutions of the full three-dimensional problem cannot be developed without complete knowledge of the vascular geometry, we seek a quasi one-dimensional simplification that relies only on the statistics of how many voxels $n(\delta)$ lie at a given distance δ from the nearest point on the vessel wall. Performing a mass balance on a differential shell of tissue at a distance δ with thickness $d\delta$ we obtain

$$D_m \left[\frac{\partial^2 C(\delta,t)}{\partial \delta^2} + \frac{1}{n(\delta)} \frac{dn(\delta)}{d\delta} \frac{\partial C(\delta,t)}{\partial \delta} \right] = \frac{\partial C(\delta,t)}{\partial t}, \qquad \textbf{[S4]}$$

subject to the boundary conditions $C(0,t) = C_v(t)$ and $C(\infty,t) = 0$ with the initial condition $C(\delta,0) = 0$. We note that Eq. **S4** readily reduces to the familiar 1D forms of the diffusion equation for planar ($n \sim \delta^0$), cylindrical ($n \sim \delta^1$) and spherical ($n \sim \delta^2$) coordinate systems.

The corresponding auxiliary problem is governed by

$$D_m \left[\frac{\partial^2 \Phi(\delta,t)}{\partial \delta^2} + \frac{1}{n(\delta)} \frac{dn(\delta)}{d\delta} \frac{\partial \Phi(\delta,t)}{\partial \delta} \right] = \frac{\partial \Phi(\delta,t)}{\partial t} \qquad \textbf{[S5]}$$

with boundary conditions $\Phi(0,t) = 1$ and $\Phi(\infty,t) = 0$ with the initial condition $\Phi(\delta,0) = 0$ where Duhamel's theorem yields the concentration for more general boundary conditions at the vessel walls as follows

$$C(\delta,t) = \int_{\tau=0}^{t} C_v(\tau) \frac{\partial \Phi(\delta,t-\tau)}{\partial t} d\tau. \qquad \textbf{[S6]}$$

We seek solutions of Eq. **S5** that reflect the following power-law variation $n(\delta) = n_1(\delta/l)^\lambda$ where l is the width of a voxel. Introducing the similarity variable $\eta = \delta/(D_m t)^{1/2}$ reduces Eq. **S5** to the following ordinary differential equation

$$\frac{d^2\Phi(\eta)}{d\eta^2} + \left(\frac{\lambda}{\eta} + \frac{\eta}{2} \right) \frac{d\Phi(\eta)}{d\eta} = 0, \qquad \textbf{[S7]}$$

which can be separated and integrated twice. Applying the boundary conditions, $\Phi(0) = 1$ and $\Phi(\infty) = 0$ to determine the constants of integration gives

$$\Phi(\eta) = \frac{\Gamma\left(\frac{1-\lambda}{2}, \frac{\eta^2}{4}\right)}{\Gamma\left(\frac{1-\lambda}{2}\right)} \qquad \textbf{[S8]}$$

for $\lambda < 1$ where $\Gamma(a,z)$ and $\Gamma(z)$ are the incomplete gamma function and complete gamma function, respectively. Values of $\Phi(\eta)$ are shown in Fig. S1 for representative values of λ. The solution given by Eq. **S8** reduces to the familiar error function result for planar geometry, that is $\lambda = 0$ yields $\Phi(\eta) = erfc(\eta/2)$.

Several elementary approximations of pharmacological importance can be readily obtained from Eq. **S8**. For example, the time that must transpire after a sudden increase (or decrease) in the

vascular concentration in order for the concentration at a given distance from the nearest vessel to reach one half of the change in the vessels is given by $1/2 = \Phi(\eta_{1/2})$. In the planar case we find that $\eta_{1/2} = \delta/(D_m t_{1/2})^{1/2} = 0.954$, whereas concave geometries ($\lambda < 0$) yield shorter times and convex geometries ($\lambda > 0$) take somewhat longer as can be seen in Fig. S1. Of further interest is the possibility that the tracer is present in the blood for a very short time relative to the duration of the diffusion processes. Here we may approximate the vascular concentration as an impulse in time yielding

$$C(\delta,t) \cong \mathrm{AUC}_v \frac{\partial \Phi(\delta,t)}{\partial t}, \qquad \textbf{[S9]}$$

where the area under the curve (AUC_v) for the concentration in the vessels is defined as

$$\mathrm{AUC}_v \equiv \int_{\tau=0}^{\infty} C_v(\tau) d\tau. \qquad \textbf{[S10]}$$

It is readily shown that the area under the curve in the vessels is identical to that in the extravascular space, but that the peak concentration $C_{\max}$ is greatly reduced as the distance from the vessel increases. Moreover, the time at which the concentration reaches its peak value $t_{\max}$ is much later as the distance from the vessel increases. For very short residence of the tracer in the vessels we obtain, respectively

$$C_{\max} \cong \mathrm{AUC}_v \frac{4 D_m \exp(-(\frac{3-\lambda}{2}))}{\Gamma(\frac{\lambda-1}{2})(\frac{3-\lambda}{2})^{\frac{3-\lambda}{2}} \delta^2} \qquad \textbf{[S11]}$$

and

$$t_{\max} \cong \frac{\delta^2}{2(3-\lambda) D_m}. \qquad \textbf{[S12]}$$

Eq. **S11** does not imply that the concentration is unbounded at the vessel walls. Instead, Eq. **S11** indicates a relative scaling with distance following a mathematically idealized impulse injection—infinite in magnitude and infinitesimal in duration. For convex and concave geometries the coefficients in Eqs. **S11** and **S12** differ slightly from the values obtained for planar geometry, but the essential dependences on distance ($C_{\max} \sim D_m/\delta^2$ and $t_{\max} \sim \delta^2/D_m$) remain unchanged. As a result, we predict that pharmacological effects expected in normal tissue will be greatly delayed and reduced in magnitude for cells abnormally distant from the nearest vessel.

The case corresponding to the random walk simulations presented in the main paper is readily obtained from the preceding analysis. The initial concentration throughout the extravascular space is uniformly C_i whereas the concentration on the vessel walls is held to zero. Here the solution is

$$\frac{C(\delta,t)}{C_i} = 1 - \Phi(\eta) = 1 - \frac{\Gamma(\frac{1-\lambda}{2}, \frac{\eta^2}{4})}{\Gamma(\frac{1-\lambda}{2})}. \qquad \textbf{[S13]}$$

The total rate of mass transfer into the vessels, which is proportional to the rate at which random walkers are absorbed on the vessel walls, can now be found by evaluating Fick's law at the vessel wall (in the limit as $\delta \to 0$) as follows

$$J(t) = D_m S \left.\frac{dC}{d\delta}\right|_{\delta=0} = \frac{C_i n_1 l^{2-\lambda} 2^\lambda D_m^{\frac{\lambda+1}{2}} t^{\frac{\lambda-1}{2}}}{\Gamma(\frac{1-\lambda}{2})} \sim t^{-\alpha}, \qquad \textbf{[S14]}$$

where S is the surface area through which diffusion takes place, that is $S = n(\delta) l^2$. By inspection, we obtain $\alpha = (1-\lambda)/2$, the formula presented in the main paper. We recognize that the flux in Eq. **S14** is mathematically unbounded for short times in the well-known, classical result ($\lambda = 0$) as well as for our new, more general case ($\lambda \neq 0$). Physically, this presents no difficulty because the boundary condition representing an instantaneous change in vascular concentration can only be approximated by changes that will actually require a finite, albeit brief, time interval.

The scaling of the residence time for the tracer (impulse response from a bolus injection similar to the clearance experiments presented in the main paper Fig. 2) can be obtained by differentiating the preceding step response with respect to time, yielding

$$h(t) = \frac{dJ(t)}{dt} \sim t^{-(3-\lambda)/2} = t^{-\alpha-1}, \qquad \textbf{[S15]}$$

where the present result exactly satisfies the classical result for a planar geometry ($\lambda = 0$ implies $\alpha = 1/2$). The exponents on time as predicted by Eqs. **S14** (step response) and **S15** (impulse response) differ by one, consistent with how the exponents in the random walk simulations on tumors in the main paper ($J(t) \sim t^{-0.73}$ for the example in Fig. 3) differ by about one from those seen in the clearance experiments ($h_{D_2O}(t) \sim t^{-1.67}$ for the example in Fig. 2).

The preceding analysis is strictly valid only when $n(\delta) \sim \delta^\lambda$ is satisfied for all $\delta > 0$, but we note that neither $n(\delta)$ nor $J(t)$ are perfect power laws throughout their respective domains. More typically, we see that $n(\delta)$ and $J(t)$ only approximate power laws over finite intervals. To investigate their local behavior we consider $\frac{d \log n(\delta)}{d \log \delta}$, which is the local value of λ and $\frac{d \log J(t)}{d \log t}$, which is the local value of $-\alpha$. Simulations using a wide variety of geometries provided later in *Numerical Simulations for Specific Geometries* demonstrate that gradual changes in λ with respect to distance are reflected in corresponding changes in α. Specifically, simulations show that $\alpha(t) \cong (1 - \lambda(\delta))/2$ where $t = \delta^2/D_m$. The simulations presented later show that this approximation is sufficiently robust to allow $\alpha(t)$ to track changes in $\lambda(\delta)$ that occur over a fraction of a decade.

The preceding analysis assumes that the tissue space is semi-infinite. Clearly, $n(\delta) \sim \delta^{-\lambda}$ cannot persist beyond $\delta_{\max}$, the greatest distance to the nearest vessels (the radius of the largest avascular space). In practice, the spatial scaling may begin to breakdown at slightly shorter distances.

Next, we consider the slowest part of the transient that occurs as diffusion into or out of the largest avascular space occurs. Again assuming one-dimensional diffusion, we can express the concentration in the largest avascular space as a sum of eigenfunctions such that

$$C(\delta,t) = \sum_{i=1}^{\infty} A_i F(\beta_i,\delta) e^{-D_m \beta_i^2 t}, \qquad \textbf{[S16]}$$

where β_is are the eigenvalues of the eigenfunctions $F(\beta_i,\delta)$ that satisfy the boundary conditions on the vessel walls. The concentration and fluxes on the surfaces depend on only the slowest decaying eigenfunction for long times. Thus, $J(t) \sim h(t) \sim e^{-D_m \beta_1^2 t}$ yielding the following expression for the time constant $t_c = 1/D_m \beta_1^2$ where β_1 is the first eigenvalue. In simple cases, the eigenvalue can be found analytically. For more complex geometries t_c can be estimated from curve-fitting numerical solutions to an exponential function at long times.

The preceding results may be used to more closely examine how flow heterogeneity and extravascular diffusion interact. We interpret the result that intravascular tracer clears more gradually from tumor ($t^{-2.29 \pm 0.20}$) than a diffusive tracer in a healthy tissue ($t^{-3.1}$) as evidence of significant flow heterogeneity in the tumors. This raises the question of how flow heterogeneity affects clearance from tumors when extravascular diffusion is present.

To address this question we explore the situation in which the vascular concentration does not approximate a mathematically ideal impulse as previously assumed, but is spread over a longer time interval that might be better approximated by $C_v(t) =$

$C_1H(t-T)t^{-\beta}$ where C_1 is a constant, $H(t-T)$ is a unit step in time that includes a transportation delay of duration T and β is the exponent that best fits the decay of the intravascular tracer concentration. Such a representation of the vascular concentration obscures details over short times, but retains the longer duration power-law behavior that we observed in our experiments where $\beta = 2.29 \pm 0.20$ (Fig. 2). We further assume that the pulse response for diffusive transport is given by $t^{-\alpha-1}e^{-t/t_c}$, which includes an interval of power-law decay followed by a more rapid exponential decay that occurs as the largest avascular space equilibrates with the vasculature. The clearance for a diffusive tracer $C_{\text{out}}(t)$ may then be approximated as

$$C_{\text{out}}(t) = \int_{\tau=0}^{t} C_1H(t-T)t^{-\beta}(t-\tau)^{-\alpha-1}e^{-(t-\tau)/t_c}d\tau. \qquad \textbf{[S17]}$$

Fig. S2 illustrates how the slowest process in a given time interval dominates, that is, the clearance curve will depend on diffusion-only $C_{\text{out}}(t) \sim t^{-\alpha-1}e^{-t/t_c}$ if $\beta > \alpha + 1$ and $t < t_c$, otherwise it will track the vascular concentration as $C_{\text{out}}(t) \sim t^{-\beta}$ when flow effects evolve more slowly. For the entire duration of our isolated tumor experiments, we found that $\beta > \alpha + 1$ ($2.29 \pm 0.20 > 1.73 \pm 0.09$) consistent with diffusion dominated transport lasting at least several hundred seconds as we observed. In contrast, the clearance reported for a highly diffusive tracer from a normal myocardium was very rapid $t^{-3.1}$ (4) indicating that diffusion effects, if present, were of short duration compared to flow effects. The capillary density of the normal myocardium is quite high and relatively uniform, yielding small $\delta_{\max}$ and $t_c < 0.1$ s for small molecules, thus placing nearly the entire clearance process in the convection dominated interval. We recognize that spatial heterogeneity in the vascular concentration can make the combined effects of flow and diffusion somewhat more complex than represented by Eq. **S17** for short times. Nonetheless, this approximate analysis helps to clarify how diffusive effects due to large unperfused regions can dominate the effects of flow patterns within the network of perfused vessels even when the arrival of tracer is delayed due to significant flow heterogeneity throughout the vascular network. The effects of flow heterogeneity on the clearance rates are further explored in *Numerical Simulations for Specific Geometries* where we present numerical simulations of fully coupled convection and diffusion in percolation networks that resemble tumor vasculature.

2 Numerical Simulations for Specific Geometries. The simulations summarized in Figs. S3 and S4 and Tables S1 and S2 show the degree to which idealized geometries and vascular images satisfy the preceding predictions. Diffusion calculations on the vascular images were performed by random walk methods, whereas those on idealized geometries were performed by finite-difference solutions of the transient diffusion equations. Finite-difference solutions were performed in Matlab using standard central differencing in space and either explicit or implicit marching in time. The various explicit and implicit integration schemes in time show modest differences in absolute accuracy, but have insignificant effects on the transport exponents. The external tissue boundaries are all taken to satisfy no flux conditions. We note that the finite-difference techniques employed here are close kin to the exact-enumeration methods often applied in the random walk approach to transport problems (2).

The most challenging test on each geometry is whether the local trends are tracked, that is, the extent to which $\alpha(t) = (1-\lambda(\delta))/2$ where $t = \delta^2/D_m$. Each plot in Figs. S3 and S4 presents results of a numerical calculation of the rate at which a diffusible substance is transferred to the blood from the extravascular space when the concentration is initially uniform everywhere, but is suddenly reduced to zero in the blood vessels by rapid convective clearance. Each plot shows the local slope of $\log(t)$ vs. $\log(J(t))$, which is $-\alpha(t)$ along with the values predicted from the local slope of $\log(\delta)$ vs. $\log(n(\delta))$ that is $-(1-\lambda(\delta))/2$. The results from finite-difference methods are relatively smooth, whereas the results from the random walks had to be averaged over short intervals to estimate the rates of change.

The range over which $\alpha(t)$ remains relatively constant indicates the power-law range. When $\alpha(t)$ undergoes a rapid drop at long times, transition to exponential behavior has begun. Experience from simulations has shown that the best linear fit of $\log(\delta)$ vs. $\log(n(\delta))$ over the interval $\delta \leq \delta_{\max}/3$ gives a reasonable value of λ to represent the power-law interval. The transition to exponential behavior begins in earnest beyond this point. Deviations between prediction and diffusion simulation at long times result from modest differences in the eigenvalues specific to each geometry. (See the estimates of $t_cD_m/\delta^2_{\max}$ in Table S1.) Deviations in $\alpha(t)$ from a constant value arise from the characteristics of the geometry. Typically, we find that $\alpha(t)$ varies somewhat more gradually than predicted from $n(\delta)$, but that local trends lasting longer than about 1/2 decade in time and 1/4 decade in length are faithfully reflected. See in particular the local variations present for a 6-generation Sierpinski carpet shown in Fig. S4. Our simulations demonstrate, that while the preceding derivation is approximate for all but the simplest planar case, it is highly robust in its ability to model a wide range of complex geometries in 2D and 3D. Imprecision introduced by the 1D approximation falls well within the range of geometric variability observed in vivo (Fig. 5*C* and Figs. S3 and S4).

Parallel Planes. Transient diffusion can be calculated exactly for arrays of parallel planes separated by the distance $2\delta_{\max}$. For short times, the space between the planes will act as a half space such that $J(t) = SC_o(D_m/\pi)^{1/2}t^{-1/2}$, that is $\alpha = 1/2$. As concentration changes approach the midpoint between the planes, the solution is better represented by the slowest decaying eigenfunction, that is $J(t) \sim e^{-t/t_c}$ where $t_cD_m/\delta^2_{\max} = 4/\pi^2$. Avascular spaces in the forms of square prisms and cubes also yield exact results $t_cD_m/\delta^2_{\max} = 2/\pi^2$ and $t_cD_m/\delta^2_{\max} = 4/3\pi^2$, respectively. Note that the time constant found numerically from the square holes in the Sierpinski carpet ($t_cD_m/\delta^2_{\max} = 0.204$) matches the prediction of $t_cD_m/\delta^2_{\max} = 2/\pi^2$ within 0.5%.

Krogh Cylinder Model. The Krogh cylinder model was based on a regular array of parallel cylinders of radius R_o that represent the tissue in the vicinity of each vessel of radius R_i (5). The outer surface of the Krogh cylinder at $\delta_{\max} = R_o - R_i$ is a boundary of symmetry between adjacent vessels. An exact analytical solution for transient diffusion can be obtained for the space between the vessel wall and the outer boundary of symmetry. Numerical solutions are also readily obtained. Whereas we do not expect that $n(\delta) \sim \delta^\lambda$ will hold exactly over any specific range of δ, we do find that local variations in $\alpha(t) = d\log J(t)/d\log t$ are well predicted by $\alpha(t) = (1-\lambda(\delta))/2$ from local changes in $\lambda(\delta) = d\log n(\delta)/d\log\delta$. In the immediate vicinity of a cylindrical surface we have $n(\delta) \sim \delta^0$ followed by a gradual transition to $n(\delta) \sim \delta^1$ as the distance from the surface increases to many radii. The exact expression for this geometry is $\lambda(\delta) = \delta/(\delta + R_i)$. Beyond the boundary of symmetry, $n(\delta)$ drops precipitously to zero. Accordingly, we expect that $\alpha(t)$ will vary so that $h(t) \sim t^{-3/2}$ and $J(t) \sim t^{-1/2}$ for short times, then tending toward $h(t) \sim t^{-1}$ and $J(t) \sim t^0$ followed by a rapid cross over into $h(t) \sim e^{-t/t_c}$ and $J(t) \sim e^{-t/t_c}$ as the outer boundary comes into play. The time constant can be found from an exact solution of the boundary value problem such that $t_c = 1/D_m\beta_1^2$ where β_1 is the first root of $J_1(\beta_1R_0)Y_0(\beta_1R_i) - J_0(\beta_1R_i)Y_1(\beta_1R_0) = 0$ where J_0, J_1, Y_0, and Y_1 are Bessel's functions. For $R_o/R_i = 5$ we find that $\beta_1R_i = 0.2824$ and $t_cD_m/\delta^2_{\max} = 0.7831$, closely matching the numerical result from a finite-difference calculation with $R_i = 40$ and $R_o = 200$ (Table S1).

Numerical results for a cylinder in a box are also presented in Table S1. This geometry corresponds to a regular array of cylinders on square centers. Because of the symmetries in this geometry, only the vicinity of one cylinder need be considered. The box side (L) equals the center-to-center spacing of the cylinders. The cylinder in a box contains a few points in the corners of the boxes that make this geometry differ slightly from the traditional Krogh cylinder.

We note that the diameter of the vessel relative to the spacing of the vessels has a small impact on λ (Table S1). Relatively small vessels lead to slightly larger values of λ if the vessel spacing is held constant. Given that tumor vessels are generally somewhat larger than normal capillaries, we would expect that λ will be slightly smaller in tumors than in normal tissues if the vessel-to-vessel distances are similar. This effect can be seen in the results from the cranial window (Fig. 5*C*) in which the tumor vessels are larger than the normal vessels, but not significantly more widely spaced.

Spherical Hole. The simplest representation of a no-flow region in 3-*D* is a spherical hole in the vasculature. For a hole of radius R_o we find $n(\delta) \sim (R_o - \delta)^2$. For small values of δ, the inner surface of the hole behaves as a planar surface yielding $n(\delta) \sim \delta^0$, $\lambda = 0$ and $\alpha = 1/2$. As the distance from the surface increases, $n(\delta)$ drops more and more rapidly as the center of the sphere is approached. There is no interval over which λ is truly constant, but a best fit obtained over the arbitrary interval $\delta \leq \delta_{\max}/3$ gives $\lambda \cong -0.28$ and a prediction that $\alpha \cong 0.64$. The eigenvalue for a spherical hole is readily found analytically, yielding $t_c D_m/\delta^2_{\max} = 1/\pi^2 \cong 0.101$.

Fractal and Quasifractal Structures. Just as a regular array of perfect cylinders is a useful, but limited, model of a healthy capillary bed, we expect that fractals and percolation clusters in particular may serve as useful, but limited, models of the more random architecture found in tumors. True fractals display scale-invariance over an infinite range. At best, blood vessels can be described as quasi-fractals, which are scale invariant in an approximate sense over a finite interval. Previous studies of 2D images found that tumor vasculature displayed scale-invariance (6–10) from roughly 50 μm to 5 mm with fractal dimensions matching those of 2D percolation clusters at the critical threshold indicating that the number and size of avascular regions in tumors was well modeled by percolation. In addition, the fractal dimension of the shortest vascular pathways in tumors was elevated similar to that in percolation implying that tumor vasculature was tortuous across many length scales. In contrast, normal vasculature was found to be more homogeneously distributed throughout the tissue with relatively straight minimum paths. Here we demonstrate the utility of the present model on finite-sized realizations of percolation clusters in 2D and 3D as well as iterated structures such as the Sierpinski carpet and Koch curve.

We created percolation networks on a square lattice at the critical threshold by several algorithms. One approach is invasion percolation. Here we begin at a site on one side of the lattice. Fictitious "strengths" are randomly assigned to each site on the lattice. Expansion of the network then proceeds by invading the weakest site neighboring the existing network. Growth is terminated when the opposite side of the lattice is reached. Alternatively, a cluster with similar scaling characteristics can be generated by randomly selecting a subset of sites on the lattice. At the critical threshold, the fraction of sites selected is sufficient to create a connected cluster that spans the available domain. Smaller, disconnected clusters are deleted.

An approximate relationship between the fractal dimension and λ can be found by considering the box-counting method for determining the fractal dimension. The number of *D*-dimensional boxes of side *S* needed to cover a surface with fractal dimension D_f scales as $N_{\text{box}} \sim S^{-D_f}$. The fraction of each box at a distance δ from the surface scales as δ^{D-1}. Therefore the overall fraction of the space at a distance δ scales as $n(\delta) \sim \delta^{D-1} N_{\text{box}}$ yielding $n(\delta) \sim \delta^{D-1} N_{\text{box}} \sim \delta^{-D_f+D-1}$. Thus we find $\lambda = D - D_f - 1$. Simulations on finite-sized objects such as the Sierpinski carpet, Koch curve and percolation clusters in 2D and 3D confirm that $n(\delta) \sim \delta^{\lambda}$ holds over a wide range of length scales. In Table S2 we compare values of λ found directly from the best fit of $n(\delta) \sim \delta^{\lambda}$ over the range $\delta \leq \delta_{\max}/3$ to estimates made from the best fit of $N_{\text{box}} \sim S^{-D_f}$ over the range ($S \leq 2\delta_{\max}/3$)—noting that a box of side $S = 2\delta$ can fit into an avascular region with a maximum distance to a vessel of δ. We note that such estimates of the box dimension are simply curve fits and do not imply strong scale-invariance. We find that estimates of λ obtained from $\lambda = D - D_f - 1$ follow the general trends seen in estimates of λ found directly from curve-fitting $n(\delta) \sim \delta^{\lambda}$, but predict α less well (Table S2).

Percolation in 3D is of particular interest because of its potential to serve as model for tumor vasculature. The 3D percolation clusters used in our numerical simulations were embedded in a relatively small domain ($64 \times 64 \times 64$) and yielded estimates of $\lambda = -0.34 \pm 0.05$. Studies of much larger clusters have found that $D_f \cong 2.54$ (2) from which we estimate $\lambda = D - D_f - 1 \cong 3 - 2.54 - 1 = -0.54$. The corresponding estimate for the time exponent $\alpha \cong 0.77$ is slightly higher than found from diffusion simulations on finite-sized 3D percolation clusters $\alpha = 0.65 \pm 0.02$ and random walks on images of small tumors (Table S1). For comparison we found that $\alpha = 0.73 \pm 0.09$ from the residence time experiments (Fig. 2) on somewhat larger tumors (about 1 mL). The time constant for the avascular space surrounding 3D percolation clusters is not available analytically, but our simulations yield $t_c D_m/\delta^2_{\max} = 0.253 \pm 0.016$.

To examine the combined effects of convection and diffusion in the presence of significant flow heterogeneity we created 2D percolation clusters on a 32×32 square lattice at the critical threshold by the invasion percolation algorithm (Fig. S5*A*). A network of blood vessels was then created by connecting neighboring sites on the percolation cluster with blood-filled tubes of uniform diameter. Flow was established in the network by introducing a pressure gradient across the network as a whole. We calculated the flow in each segment by solving the system of flow equations subject to conservation of mass at each vessel junction. The resulting networks have a relatively sparse backbone on which flow occurs, but demonstrate highly heterogeneous flow, even under the simplifying assumption of uniform vessel diameters. We note the presence of several low-resistance pathways with high blood speeds that serve effectively as arteriovenous shunts as well as a multitude of secondary, tortuous pathways that carry much slower flow. The causes and consequences of such heterogeneity and shunting are the subject of much current interest (11).

We then solved the full transient convection-diffusion equations for the concentration by standard finite-difference techniques (central differencing for diffusion, upwind differencing for convection, either explicit or implicit marching in time) with diffusion occurring throughout the entire domain and convection occurring only along the vascular pathways. The tissue boundaries at the edges of the domain were taken to satisfy no flux conditions except where blood enters or leaves the domain. Specifically, we considered the situation in which the concentration is initially uniform throughout the tumor but the concentration in the incoming blood is suddenly reduced. (By changing signs, the same model can be used for delivery at a constant infusion concentration). Fig. S5 *B–E* shows how simultaneous convection and diffusion affect the clearance of the tracer. In general, the slowest process (either convection or diffusion) dominates the response during each interval. Convection dominates at short times ($tD_m/l^2 < 1$) in Fig. S5 *B* and *C* where the diffusivity is relatively low—analogous to the intravascular tracer in the isolated tumor

experiments (Fig. 2). The outlet concentration initially follows the convection-only curve that is much steeper (larger value of α) than the diffusion-only curve. When the diffusivity is increased in Fig. S5 *D* and *E* we see that the geometrical details of the flow network are obscured by the effects of diffusion in the extravascular space—analogous to the clearance of D_2O from the isolated tumors. We note that the ratio of the diffusivity of D_2O relative that of the intravascular tracers is actually far greater than the 20:1 ratio shown here, so we did not observe diffusive effects during the clearance of the intravascular tracers in the experiments reported in Fig. 2. The time constant based on diffusion into the largest extravascular space ($t_c \sim \delta^2_{\max}/D_m$) is shown on Fig. S5 *B–E* to indicate when the effects of extravascular diffusion begin to make the transition from power-law to exponential behavior. For times beyond $t_c \sim \delta^2_{\max}/D_m$, the clearance will return to convection dominance as we observed earlier in Fig. S2 and as has been observed in the normal myocardium where the time constant is extremely short due to the close spacing of the vessels in the normal myocardium.

We now see that clearance can be convection dominated in two distinct regimes: a low-diffusivity, intravascular tracer at high flow rates or alternatively with a highly diffusive tracer in a homogeneous network with closely spaced vessels. Neither situation applies to diffusive tracers in tumors with large extravascular spaces where the effects of flow heterogeneity are not generally observable.

Vascular Images. The diffusion simulations performed on 3D vascular images display various elements of the artificial geometries considered above. Incorporating the voxel size of the original images (Table S3) allows us to plot the random walks on a physical time scale. At very short times, both normal and tumor tissues show intervals of power-law behavior with slopes near the classical diffusion result $\alpha = 1/2$. Normal tissues briefly exhibit $\alpha < 1/2$ indicating a convex extravascular space similar to that in a Krogh cylinder or regular array of cylinders. The slope of the clearance rate for tumors differs only slightly in this interval. The most pronounced difference between normal and tumor tissues is that the power-law interval lasts longer in tumors that have relatively large avascular spaces. As approximate power-law behavior persists in these tumors we find $\alpha > 1/2$ corresponding to a concave extravascular geometry such as a spherical hole or the vicinity of a percolation cluster. We note that $\alpha > 1/2$ indicates more rapid clearance than $\alpha < 1/2$, but still slower than exponential decay. Prolonging the power-law interval increases the time constant accordingly. That is, the minimum time required to change the concentration at the most distant points from the vessels increases dramatically with $\delta_{\max}$.

For small molecules ($D_m \cong 10^{-5}$ cm^2/s) we find that the actual duration of power-law behavior due to diffusion is quite short in normal tissues (less than 1 s) making it indistinguishable from convection along the vascular pathways that takes somewhat longer. Much longer power-law intervals are anticipated for larger tumors ($\delta_{\max} > 1$ mm) or for macromolecules ($D_m \cong 10^{-7}$ cm^2/s). The shape of the extravasular space has a modest effect on the time constant. The vascular images yielded $t_c D_m/\delta^2_{\max} = 0.43 \pm 0.01$, independent of the tissue type, which falls between the value for a Krogh cylinder and 3D percolation clusters, but well above the value for a spherical hole.

Overall, 3D percolation offers the most complete model of tumor vasculature by capturing the random appearance and variability of the tumor vasculature, the dispersive effects on convective transport, and the scaling features of extravascular diffusion. A spherical hole may also be of some utility as a simple geometrical model if only extravascular diffusion is of interest, but we note that the time constant is less well modeled.

The physical size of a lattice constant *l* deserves some discussion. In percolation theory, the lattice constant is the natural lower limit to the length scales over which self-similarity might be observed. In our previous study (8) we found that tumor vasculature exhibited approximate self-similarity down to a length scale of about 50 μm—roughly the mean distance between adjacent blood vessels. Below this scale, any attempt to apply methods such as box-counting will reveal features about the immediate vicinity of individual vessels, but not the scaling of the major avascular voids. Thus, we propose that the physical size of a lattice constant in a percolation model of tumor vasculature is nominally 50 μm. Using this approximation, we find that a percolation cluster in a $64 \times 64 \times 64$ domain would correspond to a 3-mm diameter tumor.

Images with finer resolution than 50 μm can be useful for studying the tortuosity and connectivity of the vascular network, but are likely to reveal little of interest with respect to the most relevant avascular spaces in tumors provided that they do not miss the existence of fine scale vessels. We note that the most important avascular spaces are the largest ones—thus making low resolution images of the entire tumor more useful than high resolution images of small segments of the tumor.

SI Materials and Methods

To test the validity of our methodology to a spectrum of normal and tumor vascular geometries, we used different transparent window models: the dorsal skinfold chamber, mammary fat pad, and cranial window (12, 13). We collected images of normal tissue from all three window models ($N = 4$ for dorsal skin chamber, $N = 5$ for mammary fat pad and $N = 19$ for cranial window). Additionally, we used two tumor cell lines: We implanted the murine mammary carcinoma MCaIV in a dorsal skinfold chamber ($N = 11$) and a mammary fat pad ($N = 4$) in severe combined immunodeficient mice and the human glioblastoma U87 in a cranial window in nude mice ($N = 52$). High resolution 3D images were collected using either Doppler optical frequency domain (14) or multiphoton imaging (15, 16). The imaging method that was used for each tissue type along with the voxel size of the images is shown in Table S3. The images typically measured ($600 \times 600 \times 150$ voxels).

1. Grebenkov DS, Filoche M, Sapoval B (2006) Mathematical basis for a general theory of Laplacian transport toward irregular interfaces. *Phys Rev E* 73:021103.
2. Ben-Avraham D, Havlin S (2000) *Diffusion and Reactions in Fractals and Disordered Systems* (Cambridge, UK, Cambridge University Press).
3. Ozisik MN (1980) *Heat Conduction* (New York, Wiley-Interscience).
4. Bassingthwaighte JB, Beard D (1995) Fractal ^{15}O-labeled water washout from the heart. *Circ Res* 77:1212–1221.
5. Krogh A (1919) The number and distribution of capillaries in muscles with calculations of the oxygen pressure head necessary for supplying the tissue. *J Physiol* 52:409–415.
6. Gazit Y, Berk DA, Leunig M, Baxter LT, Jain RK (1995) Scale-invariant behavior and vascular network formation in normal and tumor tissue. *Phys Rev Lett* 75:2428–2431.
7. Gazit Y, et al. (1997) Fractal characteristics of tumor vascular architecture during tumor growth and regression. *Microcirculation* 4:395–402.
8. Baish JW, Jain RK (2000) Fractals and cancer. *Cancer Res* 60:3683–3688.
9. Baish JW, Jain RK (2001) Untitled - reply. *Cancer Res* 61:8348–8350.
10. Craciunescu OI, Das SK, Clegg ST (1999) Dynamic contrast-enhanced MRI and fractal characteristics of percolation clusters in two-dimensional tumor blood perfusion. *J Biomech Eng* 121:480–486.
11. Pries AR, Hopfner M, le Nobel F, Dewhirst MW, Secomb TW (2010) The shunt problem: Control of functional shunting in normal and tumour vasculature. *Nat Rev Cancer* 10:587–593.
12. Jain RK, Brown EB, Munn LL, Fukumura D (2004) Intravital microscopy of normal and diseased tissues in the mouse. *Live Imaging: A Laboratory Manual*, eds. Goldman R, Spector D. (Cold Spring Harbor, NY, Cold Spring Harbor Press), pp 435–466.
13. Jain RK, Munn LL, Fukumura D (2002) Dissecting tumour pathophysiology using intravital microscopy. *Nat Rev Cancer* 2:266–276.
14. Vakoc BJ, et al. (2009) Three-dimensional microscopy of vascular networks, lymphatics, cell viability, and tissue microenvironment in vivo using optical frequency domain imaging. *Nat Med* 15:1219–1224.

15. Brown EB, et al. (2001) In vivo measurement of gene expression, angiogenesis, and physiological function in tumors using multiphoton laser scanning microscopy. *Nat Med* 7:864–868.

16. Padera TP, Stoll P, So PTC, Jain RK (2002) High-speed intravital multiphoton laser scanning microscopy of microvasculature, lymphatics, and leukocyte–endothelial interactions. *Mol Imaging* 1:9–15.

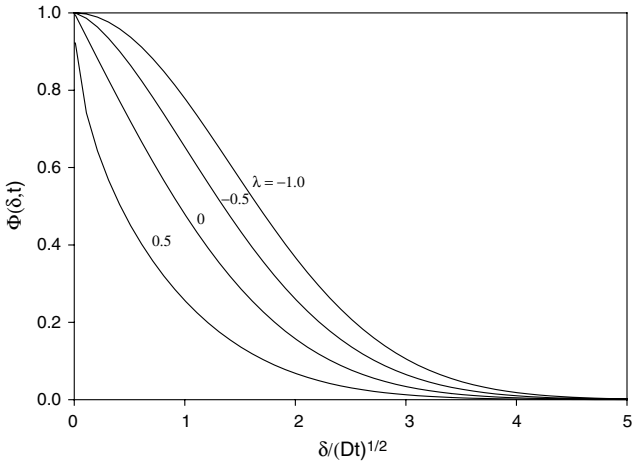

Fig. S1. Similarity solution for a step change in vascular concentration with power-law $n(\delta)$. The curve for $\lambda = 0$ corresponds to the classical error function solution for a semiinfinite planar medium.

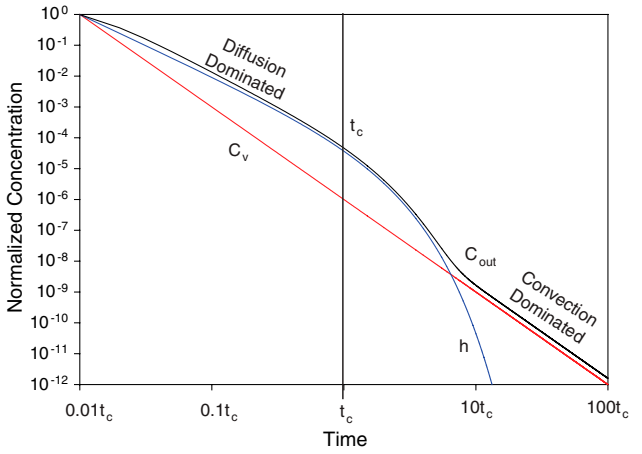

Fig. S2. Illustration of how the slowest process dominates the concentration of a tracer at the output of a tissue following a pulse input. Here we use the vascular input function $C_v(t) = t^{-3}$ and a diffusion, impulse response of $h(t) = t^{-2}e^{-t/t_c}$. The convolution is calculated using Matlab. Note how the output initially tracks $h(t)$ and then follows the vascular input function after several time constants.

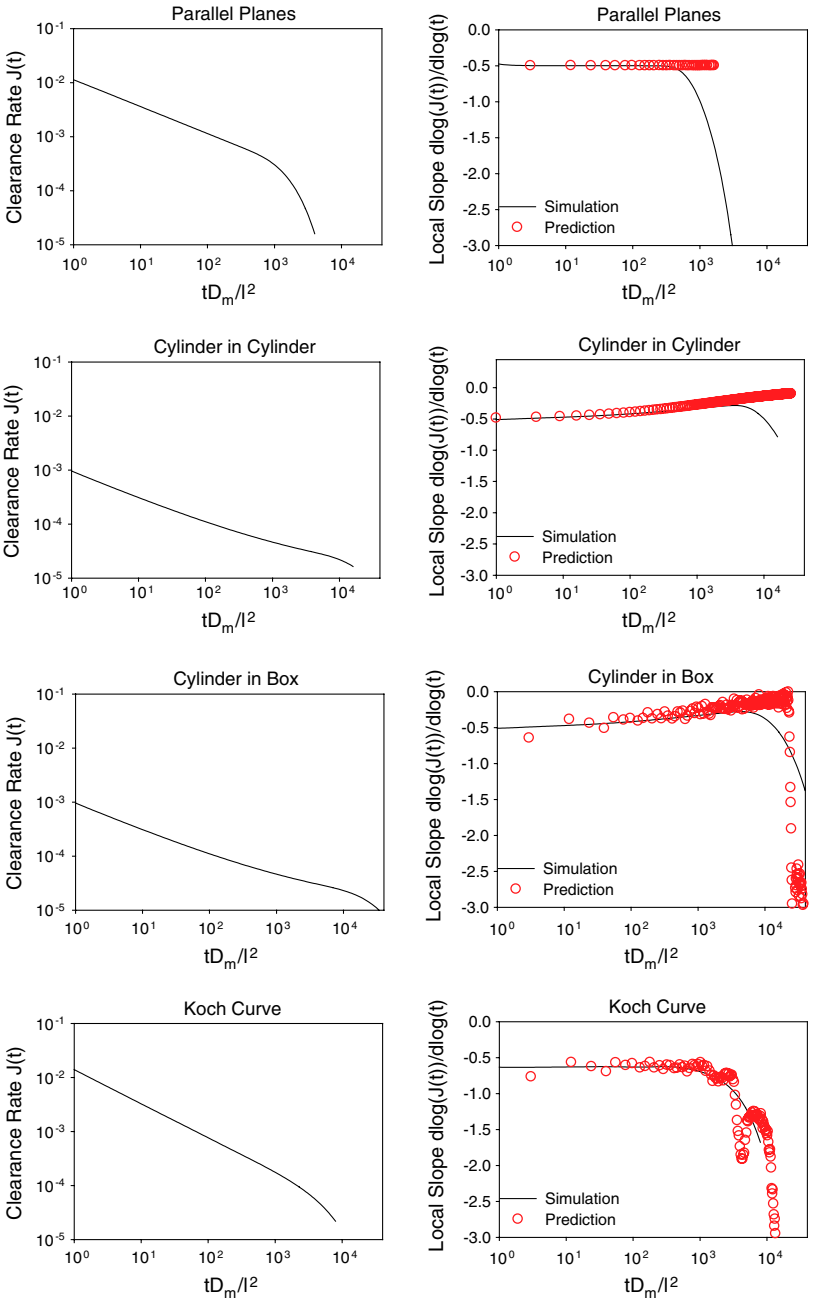

Fig. S3. Simulations of extravascular diffusion on various artificial geometries by finite-difference solution of the diffusion equation. Predictions of local slope are based on counted numbers of voxels at a given distance using $\alpha(t) = (1 - \lambda(\delta))/2$.

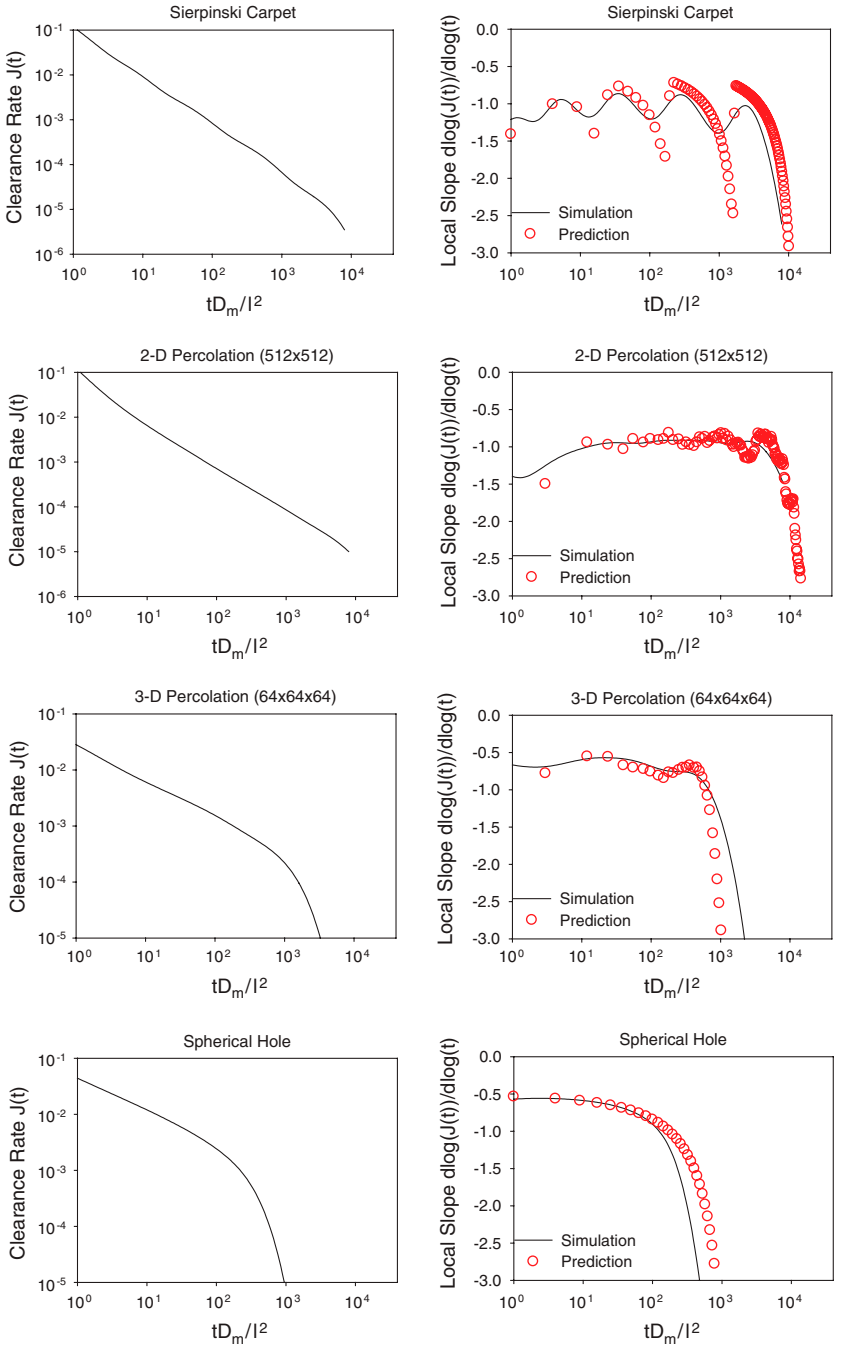

Fig. S4. Simulations of extravascular diffusion on various artificial geometries by finite-difference solution of the diffusion equation. Predictions of local slope are based on counted numbers of voxels at a given distance using $\alpha(t) = (1 - \lambda(\delta))/2$. One typical example is shown for percolation in 2 and 3 dimensions.

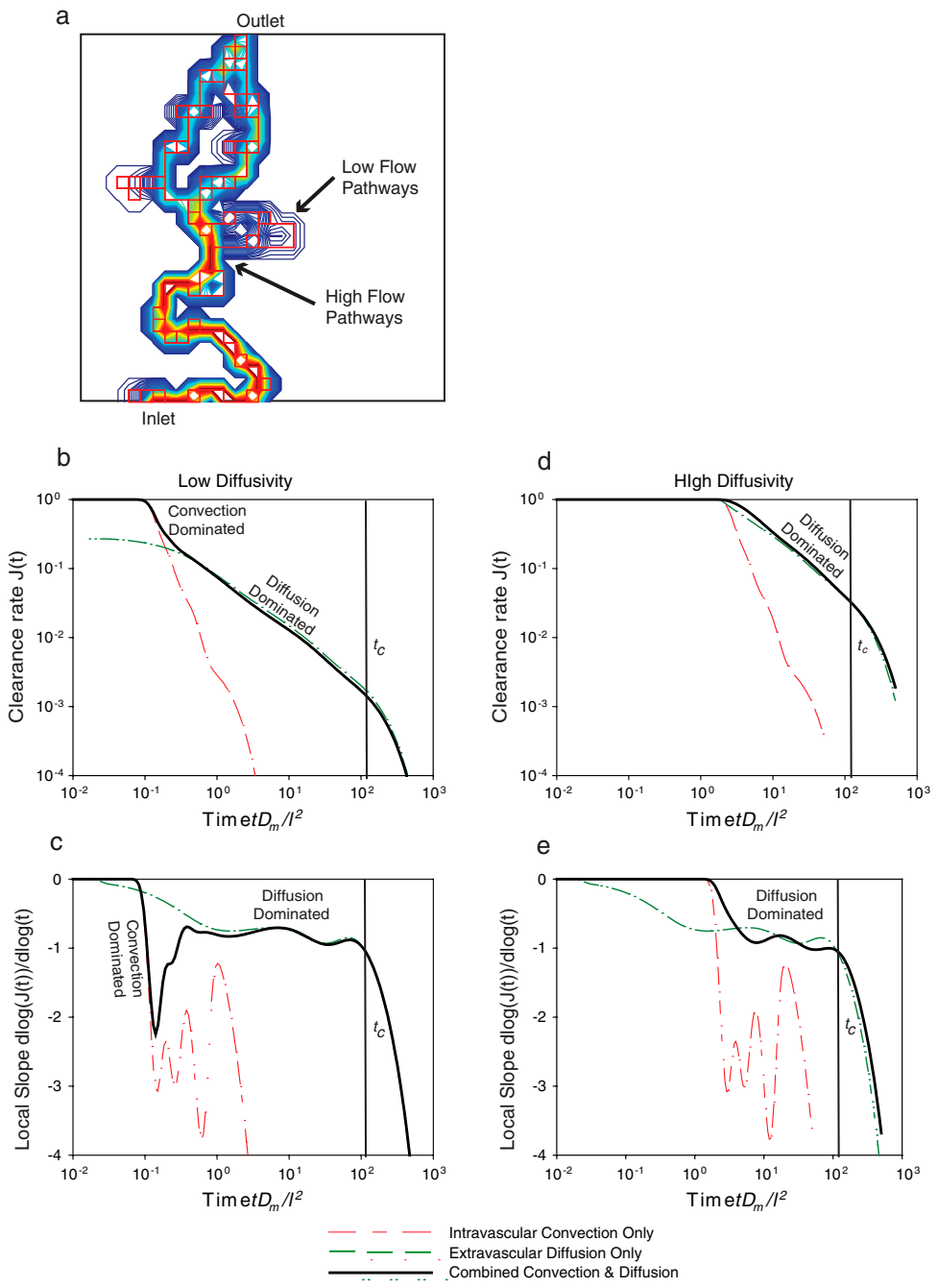

Fig. S5. Clearance from a percolation network embedded in a 32×32 two-dimensional domain. (*A*) Assuming a pressure gradient from the bottom of the domain to the top, flow occurs only on the red links of the network with the respective contours indicating relative rate of flow. Panels *B* and *C* show the concentration at the venous outlet following clearance from an initial condition in which the concentration is uniform throughout the intravascular and extravascular spaces. The inlet flow carries a zero concentration for $t > 0$. Panels *D* and *E* show the local slopes of the clearance curves. The same vascular network is used on the left and right panels with the diffusivity adjusted relative to the flow rate on the right panels by a 20:1 ratio.

Table S1. Relationship of geometric measures to time scaling

Structure	Convexity index calculated from distance statistics λ	Time exponent predicted from distance statistics $(1-\lambda)/2$	Time exponent from diffusion simulation α	Largest distance to a vessel δ_{max}	Time constant from simulation $t_c D_m/\delta^2_{max}$
Parallel planes	0.00	0.50	0.50	50	0.405
Cylinder in box ($R_i = 40$ $L = 400$)	0.31	0.35	0.38	242	0.490
Cylinder in box ($R_i = 20$ $L = 400$)	0.46	0.27	0.32	262	0.659
Cylinder in cylinder ($R_i = 40$ $R_o = 200$)	0.24	0.38	0.40	160	0.789
Cylinder in cylinder ($R_i = 20$ $R_o = 200$)	0.40	0.30	0.35	180	1.021
Spherical hole ($R_o = 40$)	−0.28	0.64	0.66	40	0.099
Koch curve (6 generations)	−0.28	0.64	0.65	158	0.190
Sierpinski carpet (6 generations)	−1.15	1.08	1.07	122	0.204
Menger sponge (4 generations)	−1.40	1.20	1.11	18	0.199
2D percolation(200×200 $N = 10$)	−0.97 ±0.09	0.98 ±0.04	0.96 ±0.04	80 ±10	0.260 ±0.017
3D percolation ($64 \times 64 \times 64$ $N = 10$)	−0.34 ±0.05	0.67 ±0.03	0.65 ±0.02	43 ±2	0.253 ±0.016
Normal subcutaneous ($N = 4$)	0.09 ±0.07	0.45 ±0.04	0.47 ±0.03	43 ±4	0.417 ±0.052
Tumor subcutaneous (MCaIV $N = 11$)	−0.49 ±0.03	0.74 ±0.02	0.70 ±0.02	142 ±8	0.410 ±0.055
Normal cranial window ($N = 19$)	0.35 ±0.04	0.33 ±0.02	0.39 ±0.02	40 ±2	0.463 ±0.023
Tumor cranial window (U87 $N = 52$)	0.13 ±0.03	0.44 ±0.02	0.46 ±0.01	42 ±2	0.429 ±0.012
Normal mammary fat pad ($N = 5$)	−0.17 ±0.02	0.58 ±0.01	0.57 ±0.01	73 ±4	0.400 ±0.025
Tumor mammary fat pad (MCaIV $N = 4$)	−0.14 ±0.06	0.57 ±0.03	0.60 ±0.03	238 ±55	0.380 ±0.056

Percolation clusters at critical thresholds.
Distances to vessels in lattice constants for artificial structures, μm for images.
Curve-fitting for convexity index $\delta \leq \delta_{max}/3$.
Curve-fitting for time exponent $t \leq (\delta_{max}/3)^2/D$.
Diffusion simulations of artificial structures done by finite differences.
Diffusion simulations of image-based structures done by random walks.
Uncertainties are 1 standard error of mean.

Table S2. Relationship of fractal dimension to convexity index

Tissue	Fractal (box) dimension from theory (T) or image (I) D_f	Convexity index calculated from fractal dimension $\lambda = D - D_f - 1$	Convexity index calculated from distance statistics λ
Koch curve (6 generations)	1.26(T)	−0.26	−0.28
Sierpinski carpet (6 generations)	1.89 (T)	−0.89	−1.15
Menger sponge (4 generations)	2.72(T)	−0.72	−1.40
2D percolation (200×200 $N = 10$)	1.89 (T)	−0.89	−0.97 ± 0.09
3D percolation ($64 \times 64 \times 64$ $N = 10$)	2.54 (T)	−0.54	−0.34 ± 0.06
Normal subcutaneous ($N = 4$)	1.82 ± 0.01 (I)	0.18 ± 0.01	0.09 ± 0.07
Tumor subcutaneous (MCaIV $N = 11$)	2.05 ± 0.02 (I)	−0.05 ± 0.02	−0.49 ± 0.04
Normal cranial window ($N = 19$)	1.96 ± 0.03 (I)	0.04 ± 0.03	0.35 ± 0.04
Tumor cranial window (U87 $N = 52$)	2.11 ± 0.02 (I)	−0.11 ± 0.02	0.13 ± 0.03
Normal mammary fat pad ($N = 5$)	1.91 ± 0.03 (I)	0.09 ± 0.03	−0.17 ± 0.02
Tumor mammary fat pad (MCaIV $N = 4$)	1.99 ± 0.05 (I)	0.01 ± 0.05	−0.14 ± 0.06

Theoretical fractal dimensions based on infinite resolution.
Curve-fitting for box dimension $S \leq 2\delta_{max}/3$.
Curve-fitting for convexity index $\delta \leq \delta_{max}/3$.
Uncertainties are 1 standard error of the mean.

Table S3. Imaging methods

Tissue type	Site	Imaging method	Voxel size (μm^3)
Normal	Dorsal skinfold chamber	Multiphoton	$2.7 \times 2.7 \times 2.5$
Normal	Mammary fat pad	Multiphoton	$2.7 \times 2.7 \times 2.5$
Normal	Cranial window	MultiPhoton	$2.5 \times 2.5 \times 5$
Tumor MCaIV	Dorsal skinfold chamber	Opt freq dom	$5 \times 5 \times 4.1$
Tumor MCaIV	Mammary fat pad	Opt freq dom	$7.62 \times 7.62 \times 4.1$
Tumor U87	Cranial window	MultiPhoton	$2.5 \times 2.5 \times 5$